Research Square

Preprints are preliminary reports that have not undergone peer review.
They should not be considered conclusive, used to inform clinical practice,
or referenced by the media as validated information.

Surface Plasmon Resonance Biosensors for Early and Accurate Diagnosis of Neurological Disorders

Ms Meenachi VR

meenachivr481@gmail.com

Sri Ramakrishna Institute of Technology

Dr Paulraj M P

Sri Ramakrishna Institute of Technology

Dr Sheela Sobana Rani K

Karpagam College of Engineering

Research Article

Keywords:

Posted Date: November 17th, 2026

DOI: https://doi.org/10.21203/rs.3.rs-7892711/v1

License: This work is licensed under a Creative Commons Attribution 4.0 International License.
Read Full License

Additional Declarations: No competing interests reported.

Surface Plasmon Resonance Biosensors for Early and Accurate Diagnosis of Neurological Disorders

***Ms Meenachi VR**
Assistant Professor, Sri Ramakrishna Institute of Technology, Coimbatore, Tamilnadu, India.
meenachivr481@gmail.com
Dr Paulraj M P
Professor, Sri Ramakrishna Institute of Technology, Coimbatore, Tamilnadu, India.
paulraj36@gmail.com
Dr Sheela Sobana Rani K
Associate Professor, Electronics and Communication Enginnering, Karpagam College of Engineering. sheelasobana5@gmail.com

Corresponding id: meenachivr481@gmail.com

Abstract— **Biosensors that use surface plasmon resonance to detect biomarkers in biofluids such as blood and cerebrospinal fluid provide hope for the accurate and early diagnosis of Alzheimer's disease. Aggregated β-amyloid as well as tau proteins are important markers of Alzheimer's disease, and our label-free biosensors can detect trace levels of these molecules. In order to detect changes in the refractive index near the sensor surface, SPR biosensors use light interacting with a thin metal coating, usually gold. Increasing the specificity and sensitivity of SPR sensors to detect several AD biomarkers is the main focus of current research. The SPR signal (usually an angle variation in the SPR curve) is affected when molecules attach to the sensor surface, which affects the refractive index. These alterations allow SPR biosensors to determine the quantity and presence of certain biomarkers. In order to dynamically track the evolution of a disease, SPR biosensors may provide real-time readings of biomarker concentrations. A more complete picture of the illness may be obtained by using SPR technology to detect many indicators concurrently. There are a number of biomarkers linked to Alzheimer's disease that SPR biosensors may detect. These include: Aβ proteins, which may be found in both soluble along with aggregated forms, play a crucial role in the pathophysiology of Alzheimer's disease. Another characteristic of Alzheimer's disease is the abnormal phosphorylated and accumulation of tau protein. Apolipoprotein E (apoE)—ADmin risk is associated with certain apoE mutations. The accuracy of diagnoses made using the CaffeNet Model may be enhanced by the capacity to identify low concentrations of biomarkers with a high degree of sensitivity. Furthermore, classification is accomplished using the Rule Learning technique. For accurate separation from diverse samples and marker identification, this plasmonic sensor only requires nanoparticles of gold and an antibody; no other procedures are required. In normal conditions, we found that the detection limit for amyloid beta (Aβ) 1–40, Aβ 1-42, and τ protein was 34.9 fM, 26 fM, and 23.6 fM, respectively, for each biomarker in the simulated blood, according to the 1, 2.23, and 3.12 nm shifts of the Rayleigh scattering peak on the shape-code plasmon system. Detecting Alzheimer's disease biomarkers has never been easier than with our first-of-its-kind very sensitive shape-code biosensor.**

Keywords— Plasmonic biosensors; Alzheimer's disease; Surface Plasmon Resonance Biosensors; CaffeNet Model; Rule Learning (RL) algorithm

I. INTRODUCTION

Deterioration in brain tissue's visuospatial memory, in particular, is associated with Alzheimer's Disease (AD), a neurodegenerative disease that develops with advancing age [1]. The evidence-based literature indicates that AD reduces life expectancy by about 50% and is a major contributor to primary memory-associated dementia, which disproportionately affects the elderly [2]. An important feature of Alzheimer's disease is the gradual shrinkage of the cerebral cortex, which is followed by neuronal dysfunction in several brain areas such as the amygdala, hippocampus, frontal base, and limbic system [3]. Despite the fact that Aβ and tau are both necessary for the development of Alzheimer's disease, frontotemporal dementia may also be caused by mutations in the tau gene, independent of any changes in Aβ [4]. Current synovial fluid levels of Aβ42, tau, while P-tau are the biomarkers associated with AD that are employed most often [5]. Upon the start of the illness, there are low amounts of Aβ42 that may be seen in CSF, but tau and P-tau values rise and become identifiable throughout the course of the disease [6]. The excellent diagnostic accuracy of the Aβ42/Aβ40 ratio makes it a credible indicator among the many known biomarkers for AD diagnosis [7]. Biosensors are analytical tools that examine bio-molecules by transforming an inherent reaction into a signal that can be measured electrically or optically [8]. There are many different kinds of transducers, but the most frequent ones include electrochemical, optical, piezoelectric, etc. fluorometry, surface-enhanced Raman spectroscopy, electrochemical biosensors, Electrochemiluminescence, and biosensors based on surface plasmon resonance are among the sensing approaches that have been used for early AD diagnosis up till this point [9]. Included in this category are label-free detection techniques, such as SPR, which function in their native states and rely on the measurement of binding-

induced changes in the refractive index (RI) [10]. Through the use of angle shifts in SPR curves arrayed on the altered gold surface, SPR analysis is able to detect even the most minute mass changes in the vicinity of the gold chip surface [11]. Thus, this detection technique permits quantitative research into biomolecular interactions and is a very straightforward and affordable way to quantify bio-molecules [12]. There has been a lot of research on SPR optic-based biosensors for the detection of AD pathologies [13]. These biosensors can sense naturally occurring chemicals in blood or cerebrospinal fluid samples, and they don't need a labeling procedure or a double antibody method [14].

Optimal outcomes and a reduction of disease progression in neurodegenerative illnesses depend on early detection. Attention: SPR related biosensors are a great tool for detecting AD biomarkers in clinical research. They are quick, sensitive, selective, and cost-effective [15].

Motivation

Deterioration of brain neurones is a hallmark of AD, a neurodegenerative disorder. As AD advances, it causes alterations in linked biomolecular levels and impacts several pathways [16]. Hence, for a more accurate diagnosis of AD, it is recommended to integrate the detection of many lesions. The τ (tau) protein, amyloid beta 1-40, and 1-42 are important markers in the pathophysiology of Alzheimer's disease and may be utilized as primary indicators for screening and diagnosis [17]. We propose a highly selective biosensor that uses unique locally tuned surface plasmon resonance to detect AD core biomarkers all on a single platform [18]. Plasmon Data Points are in Figure 1.

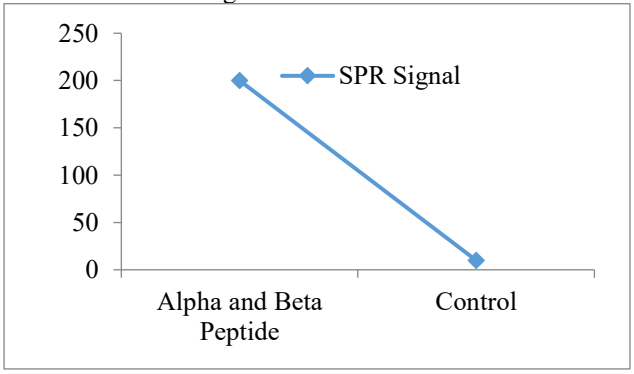


Fig.1. Plasmon Data Points

A. Aim and Scope

Sensitivity, mobility, the possibility to avoid huge sample quantities, and multiplexed detection are all appealing aspects of sensors based on electroanalytical and surface plasmon resonance technologies [19]. The analysis of several sensing protocols established in the last five years shows that both methods may be used for diagnostics. We also go into the challenges that each of these methods have that need fixing before they can be considered clinically viable [20].

II. Related Work

The low amounts of AD biomarkers in biofluids make the authors' target of [21] difficult to attain. In that study, they provide the first demonstration of using FLOWER, which stands for frequency locked optical whispering evanescent resonator, to measure the levels of Aβ42 in post-mortem cerebrospinal fluid in persons with moderate cognitive impairment, Alzheimer's disease, and a control group that was defined by clinicopathology. The diagnostic performance of FLOWER is greater than that of traditional ELISA, and it can measure CSF Aβ42 (area under curve, AUC = 0.92) while also differentiating between control and MCI samples. The power of FLOWER to screen cerebrospinal fluid samples for early detection of Alzheimer's disease is shown by their findings.

A paper-based QD aptasensor that targets amyloid beta (Aβ-42) with p-tau181 proteins via Förster Resonance Energy Transfer was created by researchers for the early detection of AD, according to their study [22]. The sensor makes use of a Whatman paper that has six detecting wells, which include both hydrophobic and hydrophilic areas, as well as hydrophobic components made of wax. The six sensing wells contains QD-aptamer-AuNP complexes, and blood samples are distributed into them after being deposited in the intake. In order to extinguish the fluorescence of CdTe QDs, target proteins cause conformational changes in aptamers. The p-tau181 and amyloid beta-42 targets are divided among four wells, with two more serving as references. The measured fluorescence emission spectra from every well demonstrate a linear relationship between the protein content and fluorescence quenching. Afterwards, the average values from the wells that target (Aβ-42) while p-tau181 are compared to the reference wells' average value, while the average values from every pair of wells are averaged. That paper-based aptasensor paves the way for individualized medication in the early detection of Alzheimer's disease and shows promise for the disease's early diagnosis.

A homogeneous plasmon-enhanced nanotransducer for localized surface plasmon resonance biosensors was constructed by accurately controlling the frameworks of double-walled nanoframes by wet chemistry, as described in [23]. Biomolecular interactions in monospace boosted by electromagnetic fields were achieved by adjusting physical characteristics in light of finite-difference time-domain simulation findings. Consequently, when it came to tau detection, DWF10 had a tenfold lower detection limit of 2.21 fM in comparison to DWF14. Notable improvement in categorizing patients with moderate cognitive impairment versus healthy controls as well as AD patients was shown, together with remarkable AUC values, suggesting further application to blood-based clinical as well as AD diagnostics. Optimizing nanoframe parameters, like the nanogap and frame thickness, to enhance sensor performance is crucial for future POCT diagnosis in response to varied detection modalities.

In order to accurately diagnose AD, the researchers in [24] created a biosensor that analyzes exomiRs in clinical blood samples using a programmable curved plasmonic nanoarchitecture. The introduction of nanospaces (such as nanocrevices and nanocavities) into the nanostructures greatly enhanced the spectral sensitivity, allowing for the attomolar detection of exomiRs in serum. That was achieved by controlling the bending angle of the plasmonic

nanostructure using sodium chloride concentration. The created biosensor differentiates between AD), moderate cognitive impairment patients, as well as healthy controls by analyzing and measuring exomiRs. Additional improvement in serum-based diagnostic performance (average accuracy of 98.22%) was seen when analyzing expression patterns of numerous exosomal biomarkers were integrated. Hence, a plasmonic biosensor that is both sensitive and accurate in detecting serum-derived exosomal biomarkers holds great promise for the early diagnosis and treatment of neurodegenerative diseases, the monitoring of cognitive decline, the conversion of mild cognitive impairment to Alzheimer's disease, and other similar conditions.

Researchers in [25] have developed a plasmonic biosensor that uses DNA-assembled advanced plasmonic architecture to reliably identify exosomal miRNAs in human blood. At localized surface plasmon resonance, the suggested nanoarchitecture outperforms nanorods by a factor of 1.66 due to its optical energy density, which is enhanced by two tiny nanogaps that produce plasmon coupling. That means that the suggested biosensor can detect exosomal miRNAs at the attomolar range with pinpoint accuracy using single nucleotide detection. Additionally, it distinguished between AD patients and healthy controls by analyzing clinical blood samples for the presence of exosomal miRNA-125b, miRNA-15a, and miRNA-361. Particularly, the optimal diagnostic performance was shown by the combination of exosomal miRNA-125b with miRNA-361, which achieved a selectivity of 95.00%, sensitivity of 91.67%, with accuracy of 99.52%. These findings show that their sensor may be used in clinical settings to diagnose AD, and it might potentially change the way dementia is studied and treated in the future.

The creation of a new electrochemical 8-well biosensor for the effective early-stage diagnosis of AD from blood was reported in [26]. The biosensor is a unique CNT-metal-porous graphene hybrid nano-interdigitated array (n-IDA). The suggested CNT-MGH n-IDA 8-well sensor was made using laser-induced graphene technology. As a first step, the suggested sensor was electrochemically characterized (electrode gap, material composition, etc.) by detecting p-aminophenol with a LOD of 0.1 picomole. In the next steps, an electrochemical enzyme-linked immunosorbent assay (e-ELISA) enzyme by-product PAP was used to diagnose Alzheimer's disease utilizing the CNT-MGH n-IDA 8-well sensor and new blood biomarkers p-Tau 217 and p-Tau 181. By interacting via the enzyme-substrate 4-aminophenyl phosphate, the electroactive ELISA by-product PAP was formed during the e-ELISA by the alkaline phosphatase enzyme linked to the detection antibody.

A new electrochemical immunosensor for KYNA detection, developed by researchers in [27], is based on a sequentially functionalized multi-electrode array. Using chronoamperometry, cyclic voltammetry, and electrochemical impedance spectroscopy, the resulting sensor was studied. The suggested biosensor has the lowest recorded limit of detection for that biomarker, detecting KYNA within a linear calibration range of 10 pM to 100 nM using CA and EIS, respectively, with a buffer LOD of 16.9 pM and 37.6 pM. In order to evaluate their device more realistically, they also evaluated the immunosensor under a human serum matrix. We found that, with diluted serum, the LOD for CA was 391.71 pM and for EIS it was 278.8 pM.

Patient heterogeneity and imprecise preclinical diagnosis are two of the main obstacles to early AD identification, according to the authors of [28]. Various biomarkers in blood and cerebrospinal fluid have been suggested to detect cerebral amyloid beta (Aβ) and tau pathology, which are symptoms of AD. There is a lot of effort going into finding powerful biomarkers for early Alzheimer's disease diagnosis and developing ultrasensitive detection methods. It is critical to understand different CSF and blood biomarkers, as well as methods for early detection, in order to reduce the global impact of AD. Neurogranin, Aβ, Neurofilament light, along with tau are some of the possible blood and CSF biomarkers that might be used to identify AD, and that article aims to provide information on the pathophysiology of AD as well as genetic and non-genetic variables linked to AD. It also mentions biomarkers that are currently being developed for AD detection. Neuroimaging, spectroscopic methods, biosensors, and neuroproteomics are just a few of the many approaches being considered for use in the early identification of AD. With that new knowledge, they may better identify early signs of AD before cognitive deterioration sets in, which might lead to the discovery of biomarkers and more effective diagnostic tools.

Recent advances in bioreceptor and bioconjugate mediated surface plasmon resonance biosensors for in vitro diagnosis of AD are discussed in that review by the investigators of [29]. The information about many significant AD biomarkers, such as Tau protein, apolipoprotein (apoE4), beta-amyloid (Aβ), 17-β-hydroxysteroid dehydrogenase type 10 (17β-HSD-10), acetylcholine, and others, is fascinatingly included in that study. Research into Alzheimer's disease biomarker detection has attracted a lot of interest, and that study elucidates the most cutting-edge techniques for bioconjugate synthesis, which have led to the creation of easy-to-implement strategies for increasing socioeconomic sensitivity. In a nutshell, that study sheds light on the analytical capabilities of bioreceptor-mediated SPR biosensors and nanoarchitectured bioconjugates, as well as the groundbreaking advantages of these technologies for the sensitive and selective in vitro identification of AD biomarkers. Overarchingly, that review provides a comprehensive synopsis of current research in the field of SPR biosensors for in vitro Alzheimer's disease diagnostics, opening the way for potential future biological applications.

A biosensor based on plasmonic asymmetric nanobridge was created by researchers in [30] to differentiate between mild cognitive impairment and AD. That biosensor could quantitatively profile phosphorylated tau proteins (p-tau) in clinical plasma samples, and it showed a strong association with the development and progression of AD. The

asymmetrical structure and conductive connection of the PAN rendered it unsynthesisable using conventional thermodynamic techniques. The biosensor is able to achieve great sensitivity, having a limit of detection in the attomolar zone for quantitative investigation of p-tau, because to PAN's unique morphological qualities, which include significant electromagnetic field enhancement. A more accurate diagnostic method was developed by identifying different p-tau species amounts in human plasma using an SVM-based machine learning algorithm. That system was able to distinguish between healthy control, MCI, and AD groups with a prediction accuracy of 94.47%. Clinical use of their suggested PAN-based plasmonic biosensor for asymptomatic phase AD progression start prediction is thus highly encouraged.

III. Proposed Work

A. Samples: Amyloid β (Aβ)

The misfolded and insoluble peptide Aβ forms cross-β-sheet super-secondary units and has a molecular weight of around 4 kDa. Theoretically, this structure is proteolysis-resistant. According to molecular research, poisonous Aβ may have a width of 70-100 A◦, and the development of neurodegenerative diseases like as AD is facilitated by the buildup of non-fibrillar Aβ assemblies.

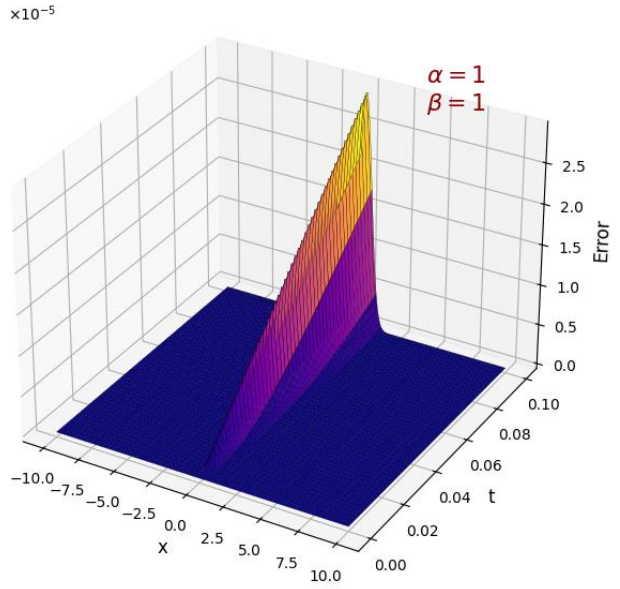


Fig.2. Data Points Alpha and Beta Model

Both the soluble Aβ40 and the insoluble Aβ42 isoforms of Aβ, which were already discussed, undergo a notable rise in AD. The molecular architectures of Aβ peptides, which aggregate into polymorphic fibrils, are highly responsive to changes in growing circumstances. Molecular structures such as oligomeric as well as protofibrillar aggregations are seen in the in vitro environment as polymorphic fibrils. Human pure Aβ fibrils vary significantly from their in vitro counterparts, according to recent structural investigation employing cryo-electron microscopy, which found that they are made up of similarly shaped protofilaments. In the supplemental materials, we also covered the clinical states and many theories pertaining to AD. Because of its capacity to monitor the very minute RI shifts on the surface of gold sensors, SPR and LSPR biosensors have brought about a major paradigm shift in the experimental settings for biomolecule detection. The beginning of Alzheimer's disease is often attributed to the increased elongation of the Aβ42 peptide in the brain cells and the subsequent decrease of the Aβ2 level to less than 500 pg/ml in CSF. So, Aβ42 is an essential biomarker for predicting how people with AD would fare. Lee and colleagues have created a very sensitive SPR-based biosensor that can detect amyloid (1-40) in CFS with a limit of detection of 1 fg/ml, and they have also suggested the use of GNPs to enhance the signal. Incorporating a variety of nanomaterials into surface plasmon resonance (SPR) biosensors leads to a notable change in the resonance angle of SPR curves. We incubated the GNPs-antibody complexes on each altered gold sensor surface for SPR signal amplification in AD detection.

Major elements assumed to be important for early identification of AD are the likelihood of amyloid fibrils aggregation as well as an increase in amyloid isoforms (1-40 and 1-42) peptide. We used an i SPR sensor-based biosensor to track amyloid levels (1-40 and 1-42) in CFS. The researchers in this work utilized a streptavidin-conjugated antibody that could detect amyloid peptides at their N-terminus in order to boost SPR signals. The amyloid peptide was detectable in the CFS samples down to 20 pM using this method. Adding silver (Ag) to SPR chips is a great way to boost the responses in systems that use SPR. While Ag oxidizes rapidly when exposed to oxygen on its own, when combined with Au metal, it becomes insoluble and exhibits a narrower line width and steeper slope in the SPR peak, resulting in enhanced SPR signals.

B. Single Sequence and Multiple Sequence

To make things easier to understand, we define "single sequence" and "multiple sequence" as follows. A time series is not anything that stands on its own. It reveals the evolution of a single characteristic or set of characteristics throughout time. A subset of time series known as a "single sequence" reflects data from a single person. The other datasets, on the other hand, include information from several individuals that are not very reliant on each other; that is, when one subject's data is changed, it does not affect the other. A "multiple sequence" or "multi-sequence" is our term for a time series that includes more than one topic.

When compared to "multivariate sequence" and "multi-dimensional sequence," the term "multiple sequence" stands out. The first, "multiple sequence," refers to a sequence that shares qualities across many subjects rather than just one; the second, "tensor sequence" or "tensor time series", are patterns that reflect many attributes rather than just one for each subject.

C. Data Pre-Processing: Global and Separate Normalization

Data normalization seeks to scale data according to a predetermined rule in order to reduce the disparity in data size. Standard deviation and mean-max scaler normalization, often known as Z-normalizing, are the two most used approaches to data normalization. In the study,

we use the min-max scaler since it is commonly employed in most previous studies.

The whole dataset may be directly normalized for individual sequences. Two methods of normalizing are shown below for several sequences.

- Global normalization

Every segment of the sequence is joined along the time axis and then normalized collectively. As an illustration, consider these two sets:

$$\{a_n\} = \{0,1,2,3,4\}$$
$$\{b_n\} = \{6,7,8,9,10\} \quad (1)$$

Both sequences transform into this using the global min-max scaler:

$$\{a'_n\} = \{0,0.1,0.2,0.3,0.4\}$$
$$\{b'_n\} = \{0.6,0.7,0.8,0.9,1\} \quad (2)$$

The range of values covered by individual sequence segments in various sequences, however, may be quite diverse (for example, one stock's price might be tens to hundreds of dollars, while another's price could be just a few dollars). Global normalization won't get rid of this variability, therefore training neural networks will still be challenging and inefficient, which will have an impact on prediction accuracy. One way to get rid of this variety is by using a process called separate normalization.

- Separate normalization

For future investigation, each segment of the sequence is normalized independently and then joined along the time dimension. Following the separate min-max scaler, the following will be the case for the sequences $\{a'_n\}$ as well as $\{b'_n\}$ mentioned earlier:

$$\{a'_n\} = \{0,0.25,0.5,0.75,1\}$$
$$\{b'_n\} = \{0,0.25,0.5,0.75,1\} \quad (3)$$

Using this approach, the variation in range between sequence parts is obviously removed. Prior to outputting, denormalization must be performed precisely, which requires recording the length of every segment in the order of sequence segment splicing and determining the maximum and minimum values of each segment, respectively.

D. Caffenet model

Three parts make up our structure. Initial step: CaffeNet, which has already been trained, extracts a number of deep features. The CaffeNet architecture consists of five convolutional layers, one pooling layer after each, and three fully linked layers at the very end. There are less layers in it than in VggNet, GoogLeNet, etc. On the other hand, categorizing aerial sceneries may suffer if the pre-trained ConvNets are too deep since the derived features become too reliant on the original dataset, ImageNet. This is why the model we provide in this study uses CaffeNet that has already been trained to handle high-resolution remote sensing images. Second, in order to pick the effective feature maps, an algorithm is developed that focuses on the complementarity of map features. In the meantime, processing several feature maps involves combining the region covariance descriptor. Lastly, we create an auxiliary descriptor to further combine the global and deep local characteristics.

Deep Local Feature Representation

Remote sensing scenes often have a top-down viewpoint, in contrast to natural photographs. This means the distribution of things in the picture is not always related to one another in space. In order to improve the accuracy and completeness of local information, this work uses the CaffeNet third- and fourth-layer output values as scene local features. Furthermore, a method is suggested for selecting feature maps that may be used to filter out feature maps from various convolutional layers. The chosen feature maps can then be fused using the area covariance descriptor, which enhances the ability to discriminate deep local features.

Covariance as a Region Descriptor

A rectangular area is denoted by R, and $Z_k(k = 1 \cdots n)$ serve as the feature points with dimensions D that fall inside the range of R. The following is the formula for calculating the covariance descriptor C_R in region R:

$$C_R = \frac{1}{(n-1)} \sum_{k=1}^{n} (Z_k - \mu)(Z_k - \mu)^T, C_R \in R^{D \times D} \quad (4)$$

where ν is the average of feature points in D dimensions Z_k,

$$\mu = \frac{1}{n} \sum_{k=1}^{n} Z_k, \mu \in R^{D \times 1} \quad (5)$$

C_R because there are three benefits to using region R's feature representation: (1) Any two feature maps at pertinent locations may be fused by computing the covariance matrix, which fuses correlated multiple features. First, fused features are much better at representing data than unfused ones. Second, the covariance matrix doesn't care about the order of the feature points, so fusion features are scale and rotation invariant. Third, the covariance matrix is symmetrical, so it doesn't matter how many dimensions a feature has. Conv_3 feature maps are discussed in this work f_{c3} and conv_4 feature maps f_{c4} first linked to build up area R_c. The computed value of R_c is the region covariance descriptor C_(R_c). Figure 2 shows the structure of R_c and the fusion of several feature points, where n_i (i=1⋯D) represents the quantity of feature maps. (n_i, n_j) $(i = 1 \cdots D, j = 1 \cdots D)$ represents the combined output of any pair of feature maps. As to CaffeNet's findings, the amount of R_c is $13 \times 13 \times 768$. Due to duplicated information

across feature maps, the discrimination of local characteristics may be compromised if the covariance matrix of R_c is derived directly. In addition, the final classification seems to have a high computational cost and feature dimensions close to 300 k.

Feature Maps Selection Algorithm

The feature maps selection method is suggested as a solution to the problems discussed above. Additionally, to ensure the method is accessible and easy to implement, f_{c3} and f_{c4} are split into n equal halves using an average channel-wise fusion technique. Equation (6) calculates the average feature map of each group.

$$FM_A(i,j) = \left(f_{avg}\left(\omega_1(i,j), \omega_2(i,j), \cdots, \omega_\beta(i,j)\right)\right) \quad (6)$$

In Equation (3), $FM_A(i,j)(1 \le i \le 13, 1 \le j \le 13)$ is the number of feature mappings and represents the element of the average feature matrix at (i,j). The function denoted as f_{avg} is the average function. Afterwards, in the same sequence, every average feature maps are merged to form a new R_c ^'. With an eye on the redundant data included in $R_c{}'$, An algorithm is developed in the following way: get the region covariance descriptor running, $C_{R_c}{}'$ of $R_c{}'$ besides transform $C_{R_c}{}'$ into the plane defined by the equation (7).

$$C_{R_c'} = V\log(\Sigma)V^T \in R^{2n\times 2n}. \quad (7)$$

in where V represents the matrix of decomposition for $C_{R_c}{}'$. For a second, the feature values in the bottom triangle of $C_{R_c}{}'$ are transformed into a vector with just one dimension. After that, we feed the SVM classifier the vector that represents each picture and make note of the classification accuracy. The third step is to choose the 2n average feature maps by considering how well they complement each other. In Algorithm 1, we can see the big picture of the algorithm.

Deep Global Feature Representation

We use characteristics from the first completely linked layer to improve the fusion of multi-scale deep features. A Q-dimensional vector is the result of the first completely linked layer, as shown in Equation (). This includes, $F_f \in R^{Q\times 1}$ is the global feature, and $X \in R^{x\times x\times l}$ stood for the last convolutional layer's feature mappings. $M_w \in R^{x\times x\times l\times Q}$ and $V_b \in R^{Q\times 1}$ act as the weight matrix and the threshold matrix, respectively. Supervised learning is a viable option for acquiring Mw, the ConvNets essential. Within, you will find a nonlinear function $\phi(\cdot)$. The truth is that selective activation functions abound. In the processing unit, we use the Rectified Linear Unit, as shown in Equation (8).

$$O_f = \begin{cases} r, & \text{if } r > 0. \\ 0, & r \le 0. \end{cases} \leftrightarrow O_f = \phi(r) = \max(0, r) \quad (8)$$
$$F_f = \phi(M_w X + V_b)$$
$$r = \sum_t w_{ij}x_t + b_f$$

where O_j and x_i denote the j-th neuron's output and the first completely connected layer's input, respectively. Prior to feature fusion, the data of F_c as well as F_f are normalized as both global and local characteristics come from various data distributions. With F_f as an instance, let's pretend that there were m samples in a dataset. The network architecture reveals that F_f has 4096 dimensions and that the dimension of the global feature matrix FM_f, which is 4096×m and made up of m samples, is 4096×m. All of a sample's global feature dimensions are represented in each column of FM_f, whereas all samples share the same feature dimension in each row. Here, we normalize the data in each row of the global feature matrices FM_f and describe it in the following way:

$$FM_f' = \left(f_1', f_2', \cdots, f_Q'\right)^T = \left(\left(\cdots, \left(f_t - f_{t_{mtan}}\right)/\left(f_{t_{max}} - f_{t_{mmin}}\right), \cdots\right)\right)^T \quad (9)$$

where f_i, f_i' depict the characteristics before to and after to normalization, correspondingly. Although. $f_{i_{max}}$ and $f_{i_{min}}$ are the highest and lowest values on the same feature matrix dimension i FM_f. It should be noted that when every value of a certain dimension is equal, $f_{i_{max}}$ is equal to $f_{i_{min}}$. In Equation (9), the divisor is 0. Therefore, for complete samples, every value of this metric is kept.

Feature Fusion and Classification

To combine the model's two streams of features, we provide a feature fusion approach that uses an element-wise addition descriptor in this work. Using the following formula, we can determine the addition descriptor:

$$F_lg = \left(\mu f_1^l \oplus (1-\mu) f_1^g, \cdots, \mu f_t^l \oplus (1-\mu) f_t^g, \cdots, \mu f_D^l \oplus (1-\mu) f_D^g\right)^T \quad (10)$$

Equation (10), where "$\oplus$ "stands for the summing function, uses F_lg as the final feature representation. f_i^l, f_i^g each represent the i-th component of the ultimate global and local characteristics, correspondingly. The weight coefficient is represented by μ, while the dimension of F_lg is D.

$$D = \max\left(\dim(F_c), \dim(F_f)\right) \quad (11)$$

This research suggests employing zero elements to extend features with lower dimensions since feature dimensions at various scales are inconsistent.

E. Empirical Mode Decomposition

The EMD method is often a quasi-orthogonal adaptive approach. In order to calculate the average enveloping line m(t), the EMD algorithm first uses all of the local extreme points of the initial signal V(t) as interpolation points. Then, the enveloping line is constructed using a cubic spline approach $m(t) = \frac{f_{max}(t)+f_{min}(t)}{2}$ (12)

where $f_{\max}(t)$ represents the boundary between the top and lower enclosing lines, while $f_{\min}(t)$ indicates the boundary below.

Taking h_1 (t) into account as the outcome of $= V(t)$ minus $m(t)$ means that:

$$h_1(t) = V(t) - m(t) \qquad (13)$$

If $h_1(t)$ terminates decomposition once it meets the IMF criterion. In cases where $h_1(t)$ fails to meet the IMF requirement, you should treat it as a new original signal and proceed as follows.

A criteria for termination must be established. The SD values of are often used as the termination criteria $h_{1k}(t)$ and $h_{1(k-1)}(t)$, i.e.,

$$SD = \sum_{t=0}^{T} \frac{(h_{1k}(t) - h_{1(k-1)}(t))^2}{h_{1k}^2(t)} \qquad (14)$$

For the purpose of determining the degree of decomposition, the orthogonal index (/O) is used:

$$IO = \sum_t \frac{\sum_{t=1}^{K} \sum_{j=1}^{K} h_l(t) h_j(t)}{V^2(t)}, i \neq j \qquad (17)$$

IO indicates how orthogonal all of the modes are to one another.

3.2. Empirical Mode Decomposition with Improvements

In order to address the issues with the EMD technique, this study introduces a better envelope fitting approach. Locate the signal's local extreme point first, and then measure the distance between each pair of neighboring extremes:

$$(t_{l\max m}, y_{l\max m}) = \left(\frac{t_{l\max} + t_{l+1\max}}{2}, \frac{y_{l\max} + y_{l+1\max}}{2}\right), i = 1,2,,,n_{\max} - 1$$
$$(t_{l\min m}, y_{l\min m}) = \left(\frac{t_{l\min} + t_{l+1\,\min}}{2}, \frac{y_{l\min} + y_{l+1\,\min}}{2}\right), i = 1,2,,,n_{\min} - 1 \qquad (15)$$

where $n_{\max}$ and $n_{\min}$ are the number of sites where the signals are at their greatest and lowest localities, respectively; the initial point of interpolation is the midpoint of the extreme points and the original extreme points, while the second derivative u^" (t) at these nodes is initially computed. If we don't know the second derivative, we may use it as a natural boundary condition: at either end, it's zero. Then, we can use the cubic spline approach to get the original envelope $u_0(t)$ following fitting.

You need to find the spot on the envelope in which the undershoot and information value are higher than the fitting value. Along the whole interval V(t), there has to be $u_0(t)$ ≥V(t). Hence, the set of undershooting regions may be represented as one where the data value in the signal exceeds the function value of the corresponding point on the envelope:

$$\left\{\left(t_{a_t'}, t_{b_t}\right) \mid V_1\left(t_{a_t}\right) = V_1\left(t_{b_t'}\right) = 0, x_1(t) > 0, t \in \left(t_{a_t'}, t_{b_t}\right), i \in \mathbf{N}\right\} \qquad (16)$$

where $V_1(t) = V(t) - u_0(t)$ where N is the total number of undershoot intervals.

Separate the non-negative real part of $x_1(t_1)$ into two sets:

$$O = \left\{o_t\left(t_{o_0}, x_1(t_0)\right), x_1(t_0) = 0, i = 1,2,\ldots\right\}$$
$$N = \left\{N_f\left(t_{n_f}, x_1 \mid \left(t_{n_f}\right)\right), x_1\left(t_{n_f}\right), x_1\left(t_{n_f}\right) > 0, j = 1,2,\ldots\right\}$$
()

If everything is perfect, the point where $u_0(t)$ meets with V(t) is still O.

By using cubic spline interpolation to match the horizontal axis of the coordinate axis using points in O and N, a new envelope, $u_1(t)$ of V(t), is generated. This is the next stage of the enhanced EMD algorithm.

Considering $u_1(t)$ as the outcome of $V(t)$ minus $u_0(t)$ means that:

$$u_1(t) = V(t) - u_0(t) \qquad (18)$$

If $u_1(t)$ terminates decomposition once it meets the IMF criterion. If the initial value of $u_1(t)$ does not meet the IMF requirement, then proceed as follows: take $u_1(t)$ as the updated original signal, and keep going until $u_1(t)$ does.

It is still the standard deviation (SD) values that determine the termination criteria, as shown in Equation (18).

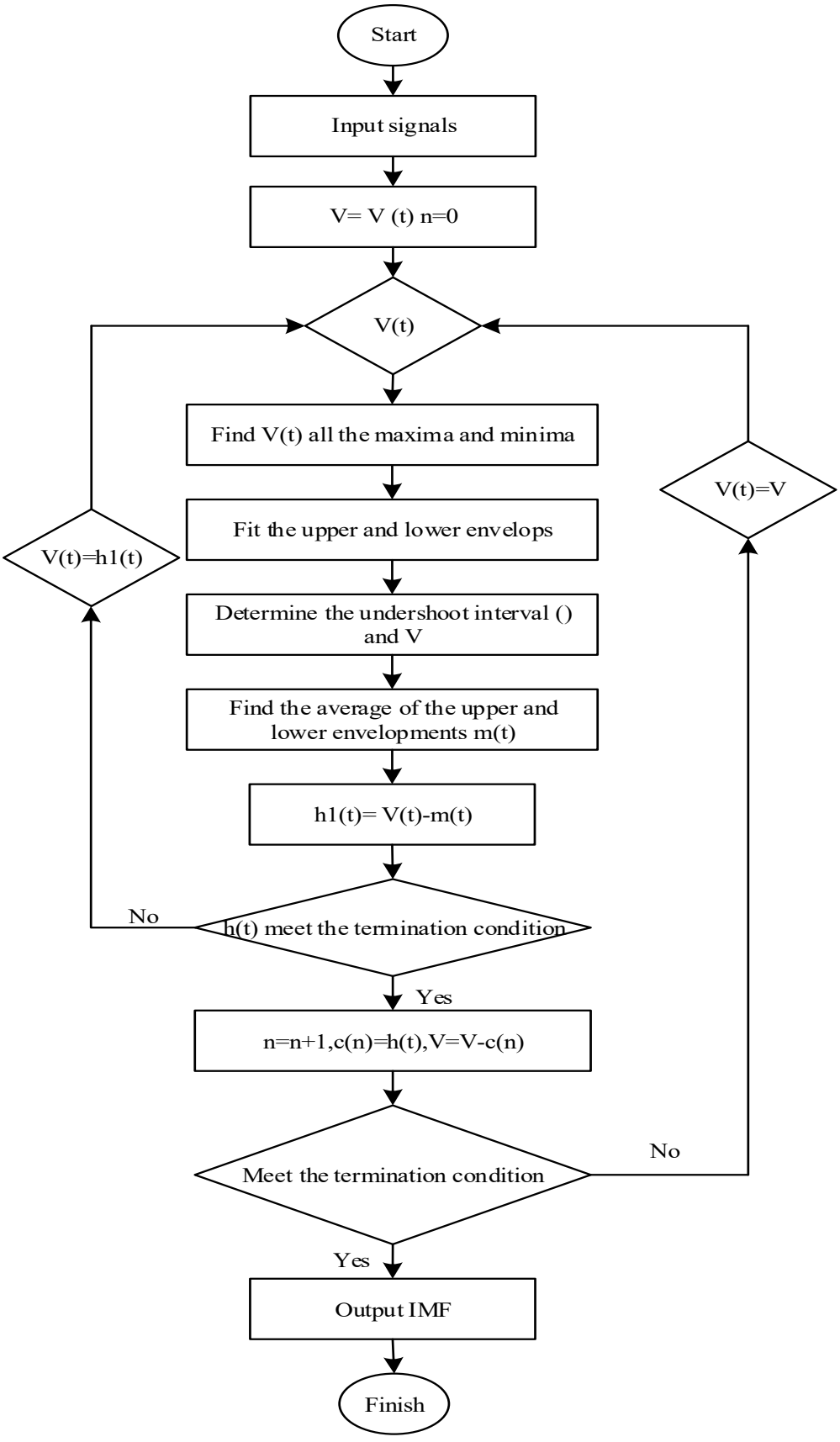


Fig.3. The schematic of the enhanced EMD algorithm.

The dimensionality of $F_l g$ is reduced by our technique as compared to concatenation. The schematic of the enhanced EMD algorithm are in Figure 3. In addition, our strategy outperforms the single scale characteristics along with other fusion features in terms of classification accuracy, according to the experimental data.

The optimization targets include the Caffenet hyper-parameters (learning rate, batch size, dropout), the SVM model hyper-parameters (maximum tree depth, subsample proportion, column subsample proportion, minimum child weight, greatest delta step, and gamma-delta), and the initial positions of each particle in the hyper-parameter search area are randomly chosen. Secondly, adaptable populations are formed by subdividing the particles. This is accomplished by finding distances to the particles with the highest local densities and then determining their local densities. After determining the value of the particle's location, we input the verification information into the model and set the hyper-parameters for prediction. Lastly, the particle fitness function is the loss function on the validation data set. A two-category issue is the simplest way to describe credit rating. Under the assumption that the labels of both positive and negative credit data samples are +1/-1, the logistic loss function may be expressed as

$$L_{\text{logistic}} = log(1 + exp(-yp)) \qquad (19)$$

here p is the value that can be predicted and y is the value that is actually measured. Due to the binary nature of our model labels in this work, the logistic loss is expressed as follows:

$$L_{\text{logistic}} = -\frac{1}{N}\sum_{t=1}^{N} \left(y_t log(p_t) + (1 - y_t) log(1 - p_t)\right) \qquad (20)$$

Based on the fitness value, the particles are categorized as either ordinary or optimum. After several update techniques have updated the associated particles' information, the algorithm verifies if the termination condition has been achieved; if it has, the optimal value is obtained. Unless the termination condition is met, the algorithm reclassifies the population based on the locations of the particles, calculates the fitness value, then updates the position data of each particle. The last step is to build the model with the best hyper-parameters, and then utilize the data for training and prediction. CaffeNet search space set are in Table 1.

Table 1. The CaffeNet search space set

Method	Hyper-Parameter	Series
CNN	Learning rate	0.1, 0.01, 0.001
	batch size	16, 32, 64, 128
	Dropout	(0.1, 0.9)

We implement supervised classification in the classification job by use of the LIBSVM package. As a kernel function, the linear function is used, and the regularization factor C is found through fivefold cross validation using the following setup $[2^{-1}, 2^{0}, \cdots, 2^{10}]$.

F. SVM Classifier

Among binary classifiers, the SVM stands out. Due to the SVM algorithm's origins in binary classification issues, it is necessary to construct a suitable multi-class classifier in order to handle multi-class situations. When problems arise with multi-class classification, two approaches may be used: the direct technique and the indirect method. Here, we use a more roundabout method by using One-Versus-Rest.

Each support vector machine in this classification technique for n categories is responsible for separating data from its respective parent categories; thus, only n support vector machines required to be built. During testing, the class that produces the highest decision function output is selected as the test sample. By resolving the subsequent optimization issue, its *ibh* SVM may be acquired.

$$\min_{\omega^t \xi^t} \frac{1}{2}(\omega^t)^T \omega^t + C\sum_{j=1}^{l} \xi_j^t \qquad (21)$$

The direction of the hyperplane is determined by the normal vector ϋ, and the distance in between the hyperplane and the distant point is determined by the displacement term b. C stands for the punishment parameter. ξ_j^i is the loss function for the hinge. The training data is I $(x_1, y_1), \ldots, (x_j, y_j)$. To see the limitations, look at Equation (22).

$$\begin{cases} (\omega^l)^T \phi(x_j) + b^l \geq 1 - \xi_j^l, & \text{if } y_j = i \\ (\omega^l)^T \phi(x_j) + b^l \leq -1 + \xi_j^l, & \text{if } y_j \neq i \\ \xi_j^l \geq 0, j = 1, \ldots, l \end{cases} \qquad (22)$$

A high-dimensional space is used to map the training data x_j by means of the ϕ function, $y_j \in \{1, \ldots, n\}$ belongs to the set x_j. The formula, when solved, produces n decision functions.

$$\begin{matrix} (\omega^1)^T \phi(x) + b^1 \\ \vdots \\ (\omega^n)^T \phi(x) + b^n \end{matrix} \qquad (23)$$

In such case, arg is the class that x belongs $\max_i [(\omega^i)^T \phi(x) + b^i]$.

The number of weed species used in this article is eight, with j ranging from one to l. To begin, one kind of weed is selected as the positive sample with the other seven is selected as the negative sample. The process continues with a different kind of weed being selected as the positive sample with the other weeds as the negative samples. At last, eight training sets are acquired and trained independently to provide eight files containing training results. In testing, these eight training outcome files are used to evaluate the associated test samples. The final result is the highest of these eight outcomes.

IV. Results & Discussion

A. Cross-Validation

The robustness of the models we developed was validated using 10-fold cross-validation. To avoid overfitting the prediction model, k-fold cross-validation is often used in machine learning. Alternatively, a model's resilience may be ascertained via k-fold cross-validation, which entails randomly selecting a dataset using a designated machine learning method. Using k-fold cross-validation, the training set is partitioned into k equal-sized subsets. The number of subsets that are produced is called the "fold" number. To construct a model, cross-validation with k folds trains k-1 subsets that stand in for the training set. The model then returns the results after applying it to the last subset, called the validation set. Our model validation performance metric was the AUC using cross-validation. We selected 10-fold cross-validation to guarantee resilience across folds, even though it is computationally costly. Additionally, the offered dataset was not very big, therefore we were capable of to control the computing demands in this investigation. Signals from Surface Plasmon Biosensors are in Figure 4. Table 2 – 4 discussed the results.

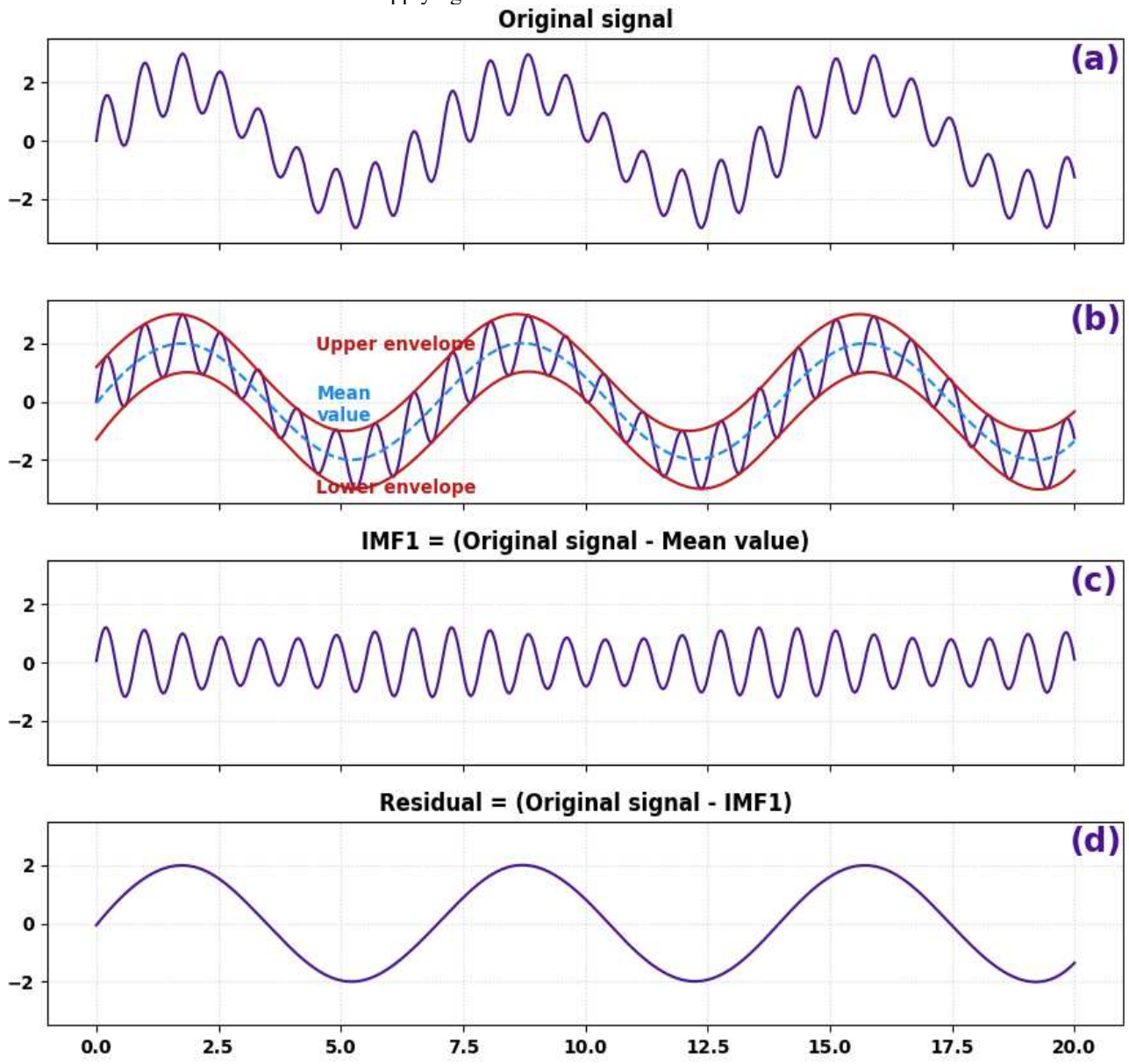


Fig.4. Signals from Surface Plasmon Biosensors

In this research, four criteria were used: MAE, RMSE, MPE, and R^2. There were no differences between the groups.

Both MAE and RMSE assess the degree to which the predicted outcomes deviate from the actual data; however, RMSE is more affected by outcomes that exhibit a high degree of inaccuracy.

$$\text{MAE} = \frac{1}{N}\sum_{t=1}^{N} |y_t - \hat{y}_t|$$
$$\text{RMSE} = \sqrt{\frac{1}{N}\sum_{t=1}^{N} (y_t - \hat{y}_t)^2} \quad (24)$$

MAPE evaluates the degree to which actual data differs from predictions.

$$\text{MAPE} = \frac{1}{N}\sum_{t=1}^{N} \left|\frac{y_t - \hat{y}_t}{y_t}\right| \quad (25)$$

The term "×100%" is removed from the formula reported in the majority of studies in order to align with the way the experimental data are presented. This is due to the fact that the "mean_absolute_percentage_error" function in Python's "sklearn. metrics" module returns decimals instead of percentages. For instance, 90% is given as 0.9. R^2 is a measure of the model's fit to the whole dataset. The model matches the data better as its value approaches 1.

$$R^2 = 1 - \frac{\sum_{t=1}^{N} (y_t - \hat{y}_t)^2}{\sum_{t=1}^{N} (y_t - \bar{y})^2} \quad (26)$$

In Equations (25) ~ (26), y_i represents the anticipated value, and is the actual value in the first sequence $\bar{y} = \sum_{i=1}^{N} y_i$. Frequency from Surface Resonance BioSensors Model are in Figure 5.

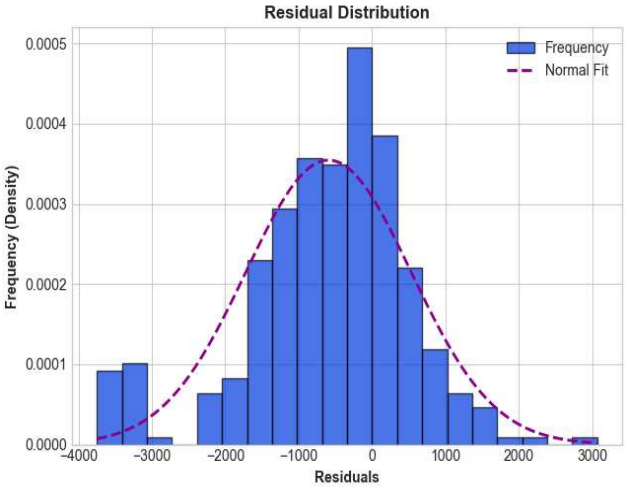
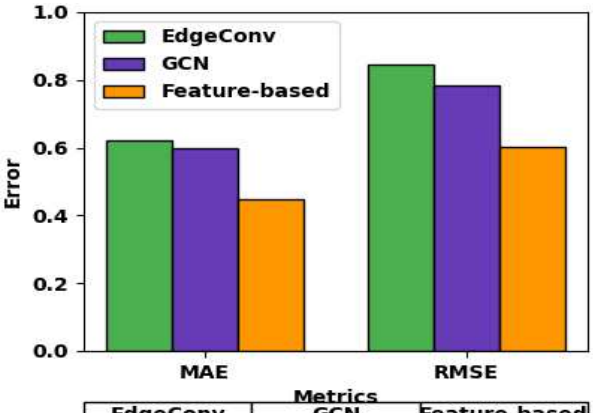
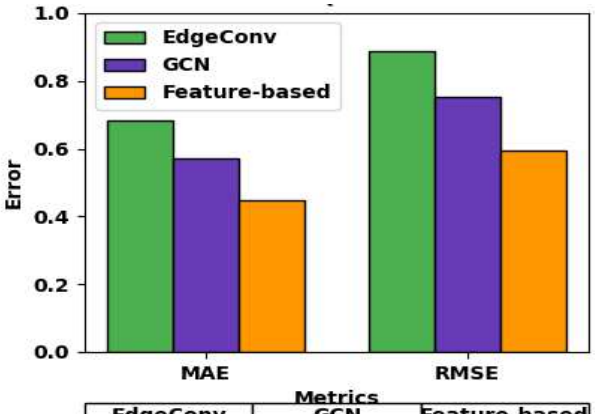


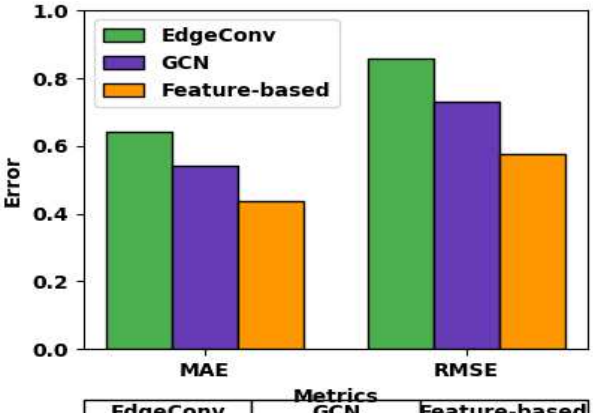
Fig.5. Frequency from Surface Resonance BioSensors Model



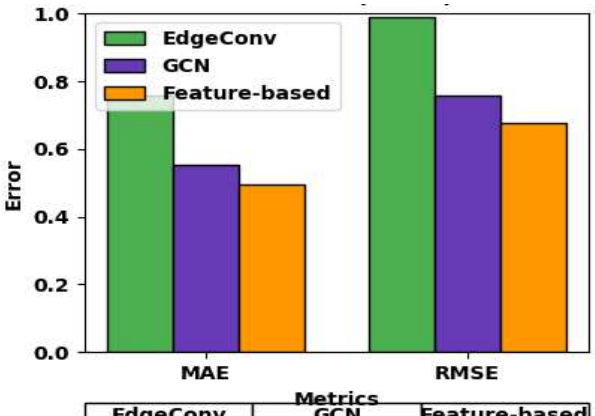
	EdgeConv	GCN	Feature-based
RMSE	0.8437	0.7823	0.6023
MAE	0.6212	0.5978	0.4494
R^2	0.8409	0.8632	0.9189



	EdgeConv	GCN	Feature-based
RMSE	0.8876	0.7517	0.5950
MAE	0.6817	0.5694	0.4492
R^2	0.8276	0.8763	0.9225



	EdgeConv	GCN	Feature-based
RMSE	0.8569	0.7318	0.5779
MAE	0.6416	0.5400	0.4390
R^2	0.8385	0.8822	0.9266



	EdgeConv	GCN	Feature-based
RMSE	0.9887	0.7564	0.6775
MAE	0.7595	0.5521	0.4953
R^2	0.8015	0.8837	0.9067

Table 2. Every decomposed subsequence of NYtem and the prediction findings of EdgeConv, GCN, and Feature Based.

Subsequences	EdgeConv			GCN			Feature Based		
	MAE	**RMSE**	**R^2**	**MAE**	**RMSE**	**R^2**	**MAE**	**RMSE**	**R^2**
RES	**0.000188**	**0.000775**	**0.997862**	0.000569	0.000145	0.998764	0.006050	0.006753	0.999786
IMF_1	0.027884	0.035799	0.221886	0.027449	0.034445	0.268336	**0.023878**	**0.032277**	**0.369336**
IMF_6	0.000997	0.001966	0.999332	0.044709	0.007196	0.904275	**0.000497**	**0.000667**	**0.998789**
IMF_7	**0.000992**	**0.001233**	**0.999669**	0.002378	0.003572	0.996490	0.005028	0.005564	0.997748
IMF_8	**0.000421**	**0.000967**	**0.998863**	0.009608	0.000867	0.998772	0.005266	0.001233	0.997975
IMF_2	0.007449	0.010335	0.918997	0.007211	0.017711	0.929969	**0.008802**	**0.099748**	**0.949655**
IMF_5	**0.000504**	**0.000432**	**0.999446**	0.001255	0.008867	0.995165	0.006607	0.002340	0.999325
IMF_3	0.000669	0.007596	0.997443	0.003196	0.005145	0.977856	**0.000997**	**0.001577**	**0.998664**
IMF_4	0.000443	0.000449	0.999567	0.007752	0.002226	0.995832	**0.000112**	**0.000775**	**0.997857**

Table 3. Comparison of Feature based's predictive performance on with and without secondary normalizing.

Subsequence	R^2 with Secondary Normalization	R^2 without Secondary Normalization
RES	0.996547	−4.207887
IMF_1	0.224439	0.209996
IMF_2	0.918675	0.915776
IMF_3	0.999568	0.997456
IMF_4	0.998532	0.999879
IMF_5	0.999788	0.999884
IMF_6	0.999846	0.999886
IMF_7	0.999788	0.999355
IMF_8	0.999966	0.998665

Table 4. Findings from the NYtem dataset experiment.

Type	RMSE	MAE	R^2	MAPE
EdgeConv	5.143866	3.913556	0.907766	0.082552
	5.108756	4.864967	0.906544	0.083228
	5.100886	3.848966	0.907337	0.082665
	5.093965	3.850332	0.907449	0.082478
	5.091644	2.848995	0.907443	0.082996
	5.211998	3.954336	0.902867	0.085558
	5.067355	3.833889	0.903365	0.091433
	5.164786	3.934997	0.904895	0.083665
	5.336968	4.073785	0.898366	0.077955
	5.328336	4.048165	0.868664	0.087336
	5.132996	3.862459	0.905922	0.083994
GCN	3.136776	3.422456	0.967885	0.051277
	3.102664	2.386997	0.969671	0.070884
	3.128216	2.393776	0.968864	0.050775
	3.086657	3.394887	0.965995	0.050996
	2.813977	2.104345	0.973458	0.012156
Feature based Model	3.183348	2.384997	0.965788	0.050459
	2.974267	2.293967	0.968445	0.048664
	2.808565	**2.093995**	**0.9718855**	**0.045574**

V. Conclusion

Aβ peptide and tau protein in plasma are two primary biomarkers identified in Alzheimer's disease. Phosphorylated tau in cerebrospinal fluid samples is also present, but to a lesser extent. One way that AD markers may be detected sensitively and selectively was by the use of optical chip-based methods, such as SPR and LSPR, in bio-recognition. Because of its capacity to quantify the very minute mass shifts on the surface of gold sensors, SPR while LSPR biosensors have caused about a major paradigm shift in the experimental settings for biomolecule detection. The numerous benefits of surface plasmon resonance biosensors—such as label-free detection, continuous monitoring, small sample volume, sensors availability, fast response time, recycling, repeatable measurements, and high sensitivity—are outweighed by their few drawbacks, such as the mass transport operation, non-specific binding, while heterogeneity on the surface locations. In addition, optical-based sensing techniques have the potential to accurately verify clinical indications and might be a perfect fit for a high-throughput platform that detects many biomarkers in AD in an ultra-sensitive and selective manner. Optical coherence tomography systems and the health care industry will undoubtedly benefit from the increased efficiency and portability of LSPR-based biosensors for Alzheimer's disease biomarkers in the future, thanks to the high surface-to-volume ratio of nanostructure arrays and other optical diagnostic devices.

Declaration:

Ethics Approval and Consent to Participate:

No participation of humans takes place in this implementation process.

Human and Animal Rights:

No violation of Human and Animal Rights is involved.

Funding:

No funding is involved in this work.

Data availability statement:

Data sharing not applicable to this article as no datasets were generated or analyzed during the current study.

Conflict of Interest:

Conflict of Interest is not applicable in this work.

Authorship contributions:

Meenachi VR - Writing- original draft, Methodology, Formal analysis.

Paulraj M P - Writing- review & editing, Conceptualization, Visualization.

Sheela Sobana Rani K - Methodology, Resources, Software.

Acknowledgement:

There is no acknowledgement involved in this work.

References

[1] Pereira, R., Oliveira, D., Pêgo, A.P., Santos, S.D., & Moreira, F.T. (2023). Electrochemical miRNA-34a-based biosensor for the diagnosis of Alzheimer's disease. Bioelectrochemistry, 154, 108553 .

[2] Miny, L., Rontard, J., Allouche, A., Violle, N., Dubuisson, L., Batut, A., Ponomarenko, A., Talbi, R., Gautier, H., Maisonneuve, B., Roux, S., Larramendy, F., Honegger, T., & Quadrio, I. (2024). Neurons as biosensors for discriminating neurological disorders in a brain-on-chip platform: Application to Alzheimer's Disease using patient CSF. bioRxiv.

[3] Brazaca, L.C., Sampaio, I., Zucolotto, V., & Janegitz, B.C. (2020). Applications of biosensors in Alzheimer's disease diagnosis. Talanta, 210, 120644 .

[4] Kim, H.J., Ahn, H.A., Kim, H., Park, D.T., Lee, J.S., Lee, B.C., Kim, J., Yoon, D.S., & Hwang, K.S. (2022). Nanoparticle-based multiplex biosensor utilising dual dielectrophoretic forces for clinical diagnosis of Alzheimer's disease. Sensors and Actuators B: Chemical.

[5] Feng, Y. (2022). Progress in Nanomaterials-based Electrochemical Biosensors for Beta-amyloid Peptides as the Biomarkers of Alzheimer's Disease. International Journal of Electrochemical Science.

[6] Le, P.G., Le, H.T., Kim, H.E., & Cho, S. (2023). SAM-Support-Based Electrochemical Sensor for Aβ Biomarker Detection of Alzheimer's Disease. Biosensors, 13.

[7] Le, P.G., Choi, S.H., & Cho, S. (2023). Alzheimer's Disease Biomarker Detection Using Field Effect Transistor-Based Biosensor. Biosensors, 13.

[8] Karki, H.P., Jang, Y., Jung, J., & Oh, J. (2021). Advances in the development paradigm of biosample‐based biosensors for early ultrasensitive detection of alzheimer's disease. Journal of Nanobiotechnology, 19.

[9] Vorobev, S.V., Yanishevskij, S.N., Emelin, A.Y., Lebedev, A.A., Lebedev, S.P., Makarov, Y., Usikov, A.S., Klotchenko, S.A., & Vasin, A.V. (2022). Prospects for the use of graphene-based biological sensors in the early diagnosis of Alzheimer's disease (review of literature). Klinicheskaia laboratornaia diagnostika, 67 1, 5-12 .

[10] Chen, H.Y., Xiao, M., He, J., Zhang, Y., Liang, Y., Liu, H., & Zhang, Z. (2022). Aptamer-Functionalized Carbon Nanotube Field-Effect Transistor Biosensors for Alzheimer's Disease Serum Biomarker Detection. ACS sensors.

[11] Bodur, O.C., Hasanoğlu Özkan, E., Çolak, Ö., Arslan, H., Sarı, N., Dişli, A., & Arslan, F.N. (2021). Preparation of acetylcholine biosensor for the diagnosis of Alzheimer's disease. Journal of Molecular Structure, 1223, 129168.

[12] Tong, J., Li, C., Zhao, J., Wang, K., Zhao, Z., Liu, Y., Qing, T., & Liu, X. (2024). Poly-Adenine Assisted Signaling Displaced Probe Ratiometric Electrochemical Aptasensor for Accurate Detection of Alzheimer's Disease Aβ Biomarkers. ACS applied materials & interfaces.

[13] Li, M., Zeng, Y., Huang, Z., Zhang, L., & Liu, Y. (2023). Vertical Graphene-Based Printed Electrochemical Biosensor for Simultaneous Detection of Four Alzheimer's Disease Blood Biomarkers. Biosensors, 13.

[14] Wang, L., Chang, M., Ma, P., Chen, H., Ma, S., Chen, N., & Zhang, X. (2023). Self-assembly of Au nanocubes for ultrasensitive detection of Alzheimer's disease biomarkers by SERS. Analytical methods : advancing methods and applications.

[15] Chakari-Khiavi, F., Mirzaie, A., Khalilzadeh, B., Yousefi, H., Abolhasan, R., Kamrani, A., Pourakbari, R., Shahpasand, K., Yousefi, M., & Rashidi, M.M. (2023). Application of Pt@ZIF-8 nanocomposite-based electrochemical biosensor for sensitive diagnosis of tau protein in Alzheimer's disease patients. Scientific Reports, 13.

[16] Negahdary, M., Sakthinathan, I., Mirsadoughi, E., Ligler, F.S., Coté, G.L., Forster, R.J., & Mabbott, S.B. (2025). Advances in biosensors for diagnosis of

Alzheimer's and Parkinson's diseases. Biosensors & bioelectronics, 284, 117535 .

[17] Kim, H.J., Choi, W., San Lee, J., Choi, J., Choi, N., & Hwang, K.S. (2021). Clinical application of serological Alzheimer's disease diagnosis using a highly sensitive biosensor with hydrogel-enhanced dielectrophoretic force. Biosensors & bioelectronics, 195, 113668 .

[18] Dey, J., Roberts, A., Mahari, S., Gandhi, S., & Tripathi, P.P. (2022). Electrochemical Detection of Alzheimer's Disease Biomarker, β-Secretase Enzyme (BACE1), With One-Step Synthesized Reduced Graphene Oxide. Frontiers in Bioengineering and Biotechnology, 10.

[19] Zhang, X., Wang, A., Wang, C., Tang, X., Jiang, Z., & Qin, J. (2023). Portable non‐enzymatic electrochemical biosensor based on caffeine for Alzheimer's disease diagnosis. View, 4.

[20] Mikuła, E. (2020). Recent Advancements in Electrochemical Biosensors for Alzheimer's Disease Biomarkers Detection. Current Medicinal Chemistry, 28, 4049 - 4073.

[21] Gin, A., Nguyen, P., Serrano, G., Alexander, G.E., & Su, J. (2024). Towards Early Diagnosis and Screening of Alzheimer's Disease Using Frequency Locked Whispering Gallery Mode Microtoroid Biosensors. Research Square.

[22] Balci, E., Yildiz, E.N., Oksuz, S.S., Ahmadli, N., Kargidan, M., Ayyildiz, N., Alemdar, E., Uludag, I., & Hasirci, U. (2024). Advancing Early Diagnosis of Alzheimer's Disease: A Paper-Based Aptasensor for Detecting Aβ(1-42) and p-tau181 from Plasma Using CdTe Quantum Dots. bioRxiv.

[23] Choi, Y.J., Haddadnezhad, M., Baek, S.J., Lee, C., Park, S., & Sim, S.J. (2024). Plasmonic Nanogap-Enhanced Tunable Three-Dimensional Nanoframes ın Application to Clinical Diagnosis of Alzheimer's Disease. ACS sensors.

[24] Song, S., Lee, J.U., Jeon, M.J., Kim, S., Lee, C., & Sim, S.J. (2023). Precise profiling of exosomal biomarkers via programmable curved plasmonic nanoarchitecture-based biosensor for clinical diagnosis of Alzheimer's disease. Biosensors & bioelectronics, 230, 115269 .

[25] Song, S., Lee, J.U., Jeon, M.J., Kim, S., & Sim, S.J. (2021). Detection of multiplex exosomal miRNAs for clinically accurate diagnosis of Alzheimer's disease using label-free plasmonic biosensor based on DNA-Assembled advanced plasmonic architecture. Biosensors & bioelectronics, 199, 113864 .

[26] Rahman, M.M., Sarkar, B., Rahman, M.T., Jin, G.J., Uddin, M.J., Bhuiyan, N.H., & Shim, J.S. (2024). Development of a highly sensitive CNT-metal graphene hybrid nano-IDA electrochemical biosensor for the diagnosis of Alzheimer's disease. Biomaterials science.

[27] Marrugo-Ramírez, J., Rodríguez-Núñez, M., Marco, M., Mir, M., & Samitier, J. (2021). Kynurenic Acid Electrochemical Immunosensor: Blood-Based Diagnosis of Alzheimer's Disease. Biosensors, 11.

[28] Rani, S., Dhar, S.B., Khajuria, A., Gupta, D., Jaiswal, P.K., Singla, N., Kaur, M., Singh, G., & Barnwal, R.P. (2023). Advanced Overview of Biomarkers and Techniques for Early Diagnosis of Alzheimer's Disease. Cellular and Molecular Neurobiology, 43, 2491 - 2523.

[29] Nangare, S.N., & Patil, P.O. (2021). Nanoarchitectured Bioconjugates and Bioreceptors Mediated Surface Plasmon Resonance Biosensor for In Vitro Diagnosis of Alzheimer's Disease: Development and Future Prospects. Critical Reviews in Analytical Chemistry, 52, 1139 - 1169.

[30] Kim, S., Ma, X., Jeon, M.J., Song, S., Lee, J.S., Lee, J.U., Lee, C., Choi, S.H., & Sim, S.J. (2024). Distinct plasma phosphorylated-tau proteins profiling for the differential diagnosis of mild cognitive impairment and Alzheimer's disease by plasmonic asymmetric nanobridge-based biosensor. Biosensors & bioelectronics, 250, 116085 .